Highly dynamic gamma-ray emissions are common in tropical thunderclouds

M. Marisaldi[1,14*], N. Østgaard[1**], A. Mezentsev[1***], T. Lang[2], J. E. Grove[3], D. Shy[3], G. M. Heymsfield[4], P. Krehbiel[5], R. J. Thomas[5], M. Stanley[5], D. Sarria[1], C. Schultz[2], R. Blakeslee[2], M. G. Quick[2], H. Christian[6], I. Adams[4], R. Kroodsma[4], N. Lehtinen[1], K. Ullaland[1], S. Yang[1], B. Hasan Qureshi[1], J. Søndergaard[1], B. Husa[1], D. Walker[6], M. Bateman[6], D. Mach[7], S. Cummer[8], M. Pazos[9], Y. Pu[8], P. Bitzer[6], M. Fullekrug[10], M. Cohen[11], J. Montanya[12], C. Younes[13], O. van der Velde[12], J. A. Roncancio[12], J. A. Lopez[12], M. Urbani[12], A. Santos[13]

[1] Department of Physics and Technology, University of Bergen, Norway
[2] NASA Marshall Space Flight Center, Huntsville, USA
[3] U.S. Naval Research Laboratory, Washington DC, USA
[4] NASA Goddard Space Flight Center, Greenbelt, USA.
[5] New Mexico Institute of Mining and Technology, USA
[6] Department of Atmospheric Science, Earth System Science Center, University of Alabama in Huntsville, Huntsville, USA
[7] Universities Space Research Association, Huntsville, AL, 35805, USA
[8] Duke University, USA
[9] Instituto de Ciencias de la Atmosfera y Cambio Climatico, UNAM, Mexico
[10] University of Bath, UK
[11] Georgia Institute of Technology, USA
[12] Polytechnic University of Catalonia, Spain
[13] Universidad Nacional de Colombia, Colombia
[14] Astrophysics and Space Science Observatory, National Institute for Astrophysics, Bologna, Italy.

*E-mail: Martino.Marisaldi@uib.no, orcid.org/0000-0002-4000-3789
**E-mail: Nikolai.Ostgaard@uib.no, orcid.org/0000-0002-2572-7033
***E-mail: Andrey.Mezentsev@uib.no, orcid.org/0000-0002-3471-7267

Thunderstorms emit fluxes of gamma rays known as gamma-ray glows[1-2], sporadically observed by aircraft[1,3-7], balloons[8-11] and from ground[12-18]. Observations report increased gamma-ray emissions by tens of percent up to two orders of magnitude above the background, sometimes abruptly terminated by lightning discharges[1,3-5]. Glows are produced by the acceleration of energetic electrons in high electric field regions within thunderclouds[8], and contribute to charge dissipation[3]. Glows had been considered as quasi-stationary phenomena[3,5,12], with durations up to a few tens of seconds and spatial scales up to 10-20 kilometers. However, no measurement of the full extension in space and time of a gamma-ray glow region and their occurring frequency have been reported so far.

Here we show that tropical thunderclouds over ocean and coastal regions commonly emit gamma rays for hours over areas up to a few thousands of square kilometers. Emission is associated with deep convective cores; it is not uniform and continuous but shows characteristic timescales of 1-10 seconds and even sub-second for individual glows. The dynamics of gamma-glowing thunderclouds starkly contradicts the quasi-stationary picture of glows, but rather resembles that of a huge gamma-glowing «boiling pot» both in pattern and behavior.

During the Airborne Lightning Observatory for FEGS and TGFs (ALOFT) aircraft campaign over Caribbean and Central America in the summer of 2023 the simplistic picture of localized and uniformly gamma-ray glowing thunderclouds was overridden. Due to a novel mission concept, where one-second resolution data were downlinked during flight, gamma-ray glowing clouds could be identified in real time, and the pilot was instructed to return to the same location until the thundercloud stopped glowing. ALOFT detected more than 500 1-to-10-second-long individual gamma-ray glows during 9 of the 10 flights, all over ocean or coastal regions (see Extended Data 10), showing that thunderclouds can emit gamma rays for hours and over huge regions.

Figure 1a shows the flight path on 24th July 2023 above a very active mesoscale convective system over southern Campeche Bay. Glows with fluxes up to ~12 times the background level (on one-second time scales) were detected during almost all the three hours spent on target (Figure 1b). Glows were detected repeatedly following consecutive passages over the same thundercloud system (see crossing trajectories and black dots in Figure 1a). The overall region including the cyan and magenta trajectories in Figure 1a was glowing for at least the 3 hours we stayed on target, starting at 05:15 UT. We do not know whether the thundercloud was glowing before we arrived and after we had to leave. The glowing region corresponds to an area of more than 9000 km^2.

Our glow observations show significant temporal variability down to the 10-millisecond time scale, overriding the previous picture of quasi-steady smoothly varying glows. Figure 2 shows successively zoomed-in observations of the gamma-ray count rate during an 8-minute-long pass and glow sequence, labelled G1 and highlighted in magenta in Figure 1 (~100 km aircraft flight distance). Figures 2c and 2e show the individual few-second-long glows (< 2 km aircraft flight distance). Figure 2f shows a “glow burst” with brightening by a factor ~3 over 20 ms, followed by a gradual flux reduction to the previous level on the same timescale. On a 1-ms timescale, this corresponds to an enhancement above the background by a factor

~30. A duration of few tens of milliseconds is three orders of magnitude lower than the typical duration of glows reported from previous observations (tens of seconds to minutes) yet is much longer than that of Terrestrial Gamma-ray Flashes (TGF) (~10 - ~100 μs), which are bright very-short transients usually associated with lightning discharges[19-22]. Transients tens of milliseconds long have been presented[23] and have been related to positron clouds. The glow burst presented here does not show any evidence for an enhanced positron annihilation line at 511 keV (see spectral analysis in Methods 4c and Extended Data 9b) and therefore must be considered as a new phenomenon. Figure 2d shows another glow that evolved into repetitive behavior termed a Flickering Gamma Flash (FGF)[24], in which the intensity is modulated in a succession of millisecond-duration spikes, separated by tens of milliseconds. Both the occurrence of FGFs and glow bursts lasting only few tens of milliseconds contradict the canonical picture of glows as quasi-static phenomena well separated from the very short transient TGFs, rather suggesting a more complex scenario linking these two phenomena.

Figure 3 shows how the glow episodes of a typical pass (in this case the cyan-highlighted episode G2 of Figure 1) are related to the storm structure, as determined by the planar cloud-top brightness temperature (Figure 3b) and the vertical reflectivity profile (Figure 3c). Together, the observations clearly indicate three convective cores producing high radar reflectivity, each 20-25 km in horizontal extent, with cloud tops extending up to ~16.5 km altitude. This implies large liquid and ice contents as well as strong convective updrafts at high altitudes in the cores. The upward-pointing electric field vectors (Figure 3c) are consistent with the charge structure of thunderclouds typically having an upper positive charge layer, which is supported also by ground observations for the flight on 29.07.2023 over Florida (see Methods 3b and Extended Data 5 and 6).

The above correlations pertain to episode G2 of the 24.07.2023 observations, but similar correlations are obtained for episode G1 and overflights of other storms, as seen in Extended Data 2 for an earlier 06.07.2023 Campeche Bay storm, and Extended Data 4 for the 29.07.2023 Florida storm. In each case the gamma-ray glow activity is remarkably temporally aligned with the overpass of successive cores, with an overall modulation in maximum intensity qualitatively consistent with the cloud-top altitude. Gamma-ray episodes over cores consisted of several (up to few tens) individual glows, often partially overlapping. The temporal profile of individual glows is typically asymmetric, with a slow rise lasting a few seconds and a fast decay (<1 s). This scenario is a common pattern observed throughout the campaign (9 of 10 flights), see Methods 3. Each glow episode (a passage over a convective core, encompassing many individual glows) is also accompanied by an increase in the local rate of electrical discharges detected by the Electric Field Change Meter (EFCM) (see Extended Data 2 and 4, and Methods 2).

To summarize, we can state with certainty that a thundercloud region can glow for hours and extend over several thousands of square kilometers. The longest continuous enhancement previously reported is 40 minutes[25] but this was only a 2% increase above background over a 1-minute time bin, not even close or comparable to the glows we report here with increases of 10-30 times the background. We can also state that each glowing episode typically lasts for about 2 minutes (20-25 km aircraft flight distance). For the individual glows (1 to ~10 s duration), however, we cannot disentangle the spatial and temporal variability components from gamma-ray observations, therefore we cannot establish the physical extent of the single source regions, whether they cover the full extent of the convective cores or if they are more compact regions within the cores. Monte Carlo simulations suggest an effective range for glow observations of 2 to ~4.5 km, depending on production altitude (see Methods 4a and

Extended Data 7). Therefore, active regions must be located within the cores. Typical rise time (2-4 seconds) and fall time (<1 second) of individual glows are too short compared to the characteristic times expected from aircraft motion towards a stationary source (see Methods 4b and Extended Data 8). Therefore, the temporal dynamics of individual glows is most likely dominated by the intrinsic time variability of the gamma-ray emission, which reflects the variability of the underlying electric field. We expect the rise time of glows to be associated with electric field increase due to convection-driven charge build-up, and the shorter fall time to be associated with electric field reduction due to charge removal following discharge processes.

In most cases, a glow flux reduction does not bring the observed flux down to the background level, but rather to an intermediate level immediately followed by a new rise phase (Figure 2c and 2e). We cannot state whether this is due to a partial discharge followed by a recharging of the same active region, or by the superposition of fluxes coming from nearby active regions within the same core. The overall time profile of glow episodes, with the brightest glows typically observed passing over the center of the convective cores (see Figure 3) suggests that most of the gamma rays do not come from a large-scale, core-sized active region, but rather from one or more compact regions concentrated towards the center of the cores. For the sub-second glow bursts with only tens of millisecond rise and fall times we can with high confidence state they are due to temporal variability of the source region.

The observations suggest what we call 'the boiling pot analogy'. Gamma-ray glowing regions are tightly associated to strong convective cores, with several individual cores evolving during the development and mature phases of tropical thunderstorms. Local gamma-ray emission follows the lifetime of the associated core, but particularly with large multicell storms the overall gamma-ray glowing region can last for hours and extend over thousands of square kilometers, tightly matching the most active regions of the storm.

So far, modeling efforts have been based on simplistic assumptions on the extent of the glow region and electric field configurations[26-27], namely uniform and constant electric field extended over large (several square km) regions. Our observations prompt the need to go beyond this simplistic static representation of glows. Inhomogeneous charge structure and its temporal dynamics must be considered in realistic simulations. The pervasiveness of gamma-ray emission over large time and spatial scales in ocean and coastal tropical thunderclouds has a broad range of implications, barely touched on in previous studies, spanning from their effects on cloud discharge[3], alteration of the local environment due to isotope production[28], and potential effect on cloud chemistry and dynamics.

REFERENCES

1. Parks, G.K., et al., *X-ray enhancements detected during thunderstorm and lightning activities.* Geophysical Research Letters, **8**(11): p. 1176-1179 (1981).
2. Dwyer, J.R., D.M. Smith, and S.A. Cummer, *High-Energy Atmospheric Physics: Terrestrial Gamma-Ray Flashes and Related Phenomena.* Space Science Reviews, **173**(1-4): p. 133-196 (2012).
3. Kelley, N.A., et al., *Relativistic electron avalanches as a thunderstorm discharge competing with lightning.* Nat Commun, **6**: p. 7845 (2015).
4. Ostgaard, N., et al., *Gamma Ray Glow Observations at 20-km Altitude.* Journal of Geophysical Research-Atmospheres, **124**(13): p. 7236-7254 (2019).

5. Kochkin, P., et al., *In-Flight Observation of Gamma Ray Glows by ILDAS.* Journal of Geophysical Research-Atmospheres, **122**(23): p. 12801-12811 (2017).
6. McCarthy, M. and G.K. Parks, *FURTHER OBSERVATIONS OF X-RAYS INSIDE THUNDERSTORMS.* Geophysical Research Letters, **12**(6): p. 393-396 (1985).
7. McCarthy, M.P. and G.K. Parks, *ON THE MODULATION OF X-RAY FLUXES IN THUNDERSTORMS.* Journal of Geophysical Research-Atmospheres, **97**(D5): p. 5857-5864 (1992).
8. Eack, K.B. and W.H. Beasley, *Long-duration X-ray emissions observed in thunderstorms.* Journal of Geophysical Research: Atmospheres, **120**(14): p. 6887-6897 (2015).
9. Eack, K.B., et al., *X-ray pulses observed above a mesoscale convective system.* Geophysical Research Letters, **23**(21): p. 2915-2918 (1996).
10. Eack, K.B., et al., *Initial results from simultaneous observation of X rays and electric fields in a thunderstorm.* Journal of Geophysical Research-Atmospheres, **101**(D23): p. 29637-29640 (1996).
11. Eack, K.B., et al., *Gamma-ray emissions observed in a thunderstorm anvil.* Geophysical Research Letters, **27**(2): p. 185-188 (2000).
12. Wada, Y., et al., *Catalog of gamma-ray glows during four winter seasons in Japan.* Physical Review Research, **3**(4) (2021).
13. Chilingarian, A., *Thunderstorm ground enhancements-Model and relation to lightning flashes.* Journal of Atmospheric and Solar-Terrestrial Physics, **107**: p. 68-76 (2014).
14. Chilingarian, A., B. Mailyan, and L. Vanyan, *Recovering of the energy spectra of electrons and gamma rays coming from the thunderclouds.* Atmospheric Research, **114-115**: p. 1-16 (2012).
15. Chilingarian, A., G. Hovsepyan, and A. Hovhannisyan, *Particle bursts from thunderclouds: Natural particle accelerators above our heads.* Physical Review D, **83**(6) (2011).
16. Chilingarian, A., G. Hovsepyan, and L. Vanyan, *On the origin of the particle fluxes from the thunderclouds: Energy spectra analysis.* EPL (Europhysics Letters), **106**(5) (2014).
17. Tsuchiya, H., et al., *Hardening and Termination of Long-Duration γ Rays Detected Prior to Lightning.* Physical Review Letters, **111**(1) (2013).
18. Tsuchiya, H., et al., *Long-durationγray emissions from 2007 and 2008 winter thunderstorms.* Journal of Geophysical Research, **116**(D9) (2011).
19. Smith, D.M., et al., *Terrestrial gamma-ray flashes observed up to 20 MeV.* Science, **07**(5712): p. 1085-8 (2005).
20. Marisaldi, M., et al., *Detection of terrestrial gamma ray flashes up to 40 MeV by the AGILE satellite.* Journal of Geophysical Research: Space Physics, **115**(A3) (2010).
21. Briggs, M.S., et al., *First results on terrestrial gamma ray flashes from the Fermi Gamma-ray Burst Monitor.* Journal of Geophysical Research: Space Physics, **115**(A7) (2010).
22. Ostgaard, N., et al., *First 10 Months of TGF Observations by ASIM.* Journal of Geophysical Research-Atmospheres, **124**(24): p. 14024-14036 (2019).
23. Dwyer, J.R., et al., *Positron clouds within thunderstorms.* Journal of Plasma Physics, **81**(4) (2015).
24. Østgaard, N.; Mezentsev, A.; Marisaldi, M.; Grove, J. E.; M. Quick, M.; et al., *Flickering Gamma-Ray Flashes, the Missing Link between Gamma Glows and TGFs.* Nature, this issue (2024).
25. Tsuchiya, H., et al., *Observation of thundercloud-related gamma rays and neutrons in Tibet.* Physical Review D, **85**(9), (2012).
26. Sarria, D., et al., *Library of Simulated Gamma-Ray Glows and Application to Previous Airborne Observations.* Journal of Geophysical Research-Atmospheres, **128**(9) (2023).
27. Wada, Y., et al., *Negative Excursion of Surface Electric Fields During Gamma-Ray Glows in Winter Thunderstorms.* Journal of Geophysical Research: Atmospheres, **128**(21): p. e2023JD039354 (2023).
28. Enoto, T., et al., *Photonuclear reactions triggered by lightning discharge.* Nature, **551**(7681): p. 481-484 (2017).

FIGURE LEGENDS

Fig. 1. Map and gamma-ray sequence for the flight on 24.07.2023.
a) Flight trajectory (grey) overlaid on GOES-18 infra-red temperatures, along with marked gamma-ray fluxes exceeding 25% above the background level (black dots). The magenta trajectory corresponds to the glow episodes plotted in Figure 2b, also marked as G1 in panel b. The cyan trajectory corresponds to the glow episodes plotted in Figure 3, also marked as G2 in panel b. For both trajectories the direction of motion of the plane is from left to right. The brightness temperature cloud image corresponds to time 07:24:251 UT, close to the maximum emission in the cyan region. b) BGO count rate. Time on target: 05:00 UT – 08:20 UT.

Fig. 2. Gamma-ray glow temporal variability.
a) BGO (black) and iSTORM (red) count rates (1s bin) for 24.07.23. b) zoomed view (100 ms bin) for the 10-minutes time interval highlighted in black in panel a, corresponding to time interval G1 highlighted in magenta in Figure 1. c, e) zoomed view (10 ms bin) for the 8-seconds time intervals highlighted in black in panel b. d, f) zoomed view (1 ms bin) for the 1-second time intervals highlighted in black in panel c and e, respectively.

Fig. 3. Sequence of glows with simultaneous electric field and cloud characterization data.
Time interval G2 on 24.07.2023 highlighted in cyan in Figure 1. a) BGO count rate. b) Brightness Temperature (TB) from the Advanced Microwave Precipitation Radiometer (AMPR) 85.5 GHz Channel A. Sweep Index 0 (49) corresponds to scan direction 45 degrees from Nadir towards starboard (port). c) vertical radar reflectivity profile from the X-band radar (EXRAD). Black vectors are the E_{xz} component of the electric field from the Lightning Instrument Package (LIP), where x-axis is the direction of motion and z-axis is the upward-pointing vertical direction. AMPR, EXRAD and LIP (see Method 2) data are not shown if roll angle is larger than 2 degrees (aircraft maneuvering).

Acknowledgements

This work made use of data from UIB-BGO, iSTORM, EXRAD, AMPR, LIP, EFCM, from the ALOFT instrument suite, VHF data from the Central Florida Lightning Mapping Array (CFLMA), and ABI data from GOES-16 and GOES-18.
The ALOFT campaign and the UIB-BGO instrument was supported by European Research Council under the European Union's Seventh Framework Programme (FP7/2007–2013)/ERC grant agreement no. 320839 and the Research Council of Norway under contracts 223252/F50 (CoE) and contract 325582. Some of the simulations were performed on resources provided by UNINETT Sigma2—the National Infrastructure for High Performance Computing and Data Storage in Norway, under project no. NN9526K. Work at NRL on ALOFT is supported by the Office of Naval Research 6.1 funds. In addition, D. Shy is supported by the U.S. Naval Research Laboratory's Jerome and Isabella Karle Fellowship. The New Mexico Tech authors acknowledge NSF Grants 1720600 and 2214044, Robert Brown of the University of Central Florida for setting up and operating the CFLMA stations, and William Rison for providing the data. The participation of J.A.R, J.L., M.U., O.vdV. and J.M. and the fielding of instruments on San Andrés island was supported by projects EQC2021-006957-P and PID2022-136348NB-C33 by the government of Spain (MCIN/AEI/10.13039/501100011033) and the European Regional Development Fund "ERDF - A way of making Europe" by the European Union. M.F. was sponsored by the Royal Society (UK) grant NMG/R1/180252 and the Natural Environment Research Council (UK) under grants NE/L012669 /1 and NE/H024921/1. S.A.C. and Y.P. were partly supported by the National Science Foundation Dynamic and Physical Meteorology program through Grant AGS-2026304. The authors thank the NASA ER-2 Project Team at NASA Armstrong Flight Research Center, for supporting the ALOFT campaign, and the MacDill Air Force Base for hosting. Significant financial and logistical support for ALOFT was provided by the NASA Earth Science Division. We thank the governments of Mexico, Bahamas, Colombia, Belize, Guatemala, Honduras, Nicaragua, Panama, Dominican Republic, Costa Rica, El Salvador, Haiti, Turks & Caicos, Jamaica, and the Cayman Islands for approving ER-2 overflights in support of ALOFT. GOES MDS sectors in support of ALOFT were enabled by NOAA. The FEGS and EFCM team acknowledge the work of Scott Podgorny, David Corredor, and Mike Stewart. For AMPR we thank Douglas Huie (UAH), Corey Amiot (NASA Postdoctoral Program), and Eric Cantrell (NASA MSFC). We acknowledge the High-altitude Radar group at NASA Goddard that provided data including Matthew McLinden, Lihua Li, Peter Pantina, and Charles Helms.

Author Contributions

M.M, N.O. and A.M. have led this study. The ALOFT campaign was led by N.O., T.L. M.M. and C.S. The UIB-BGO instrument was provided by N.O., M.M., K.U., S.Y., B.H.Q, J.S and B.H. and analyzed by A.M., N.O., M.M., D.S., N.L. The iSTORM data were provided and analyzed by J.E.G., D.S. and D. W. The AMPR data were provide by T.L. The EXRAD data were provided by G.H. The LIP data were provided by C.S, D.M. and M.B. The EFCM data were provided by H.C. and R.B. The CFLMA data was analyzed by P.K., R.T., and M.S. Additional radar and radiometric data for the entire campaign were provided by I.A. and R.K. Additional ground radio stations were operated for the entire campaign by S.A.C., Y.P., M.P., P.B., M.F., M.C., J.M, C.Y., O.vdV., J.A.R, J.A.L., M.U. and A.S.

Competing Interests The authors declare that they have no competing financial interests.

Correspondence Correspondence and requests for materials should be addressed to M. Marisaldi (Martino.Marisaldi@uib.no), N. Østgaard (Nikolai.Ostgaard@uib.no) and A. Mezentsev (Andrey.Mezentsev@uib.no).

METHODS

1. THE ALOFT FLIGHT CAMPAIGN

The Airborne Lightning Observatory for FEGS* and TGFs (ALOFT) is an aircraft campaign conducted during the month of July 2023 with a NASA ER-2 aircraft based at the McDill Air Force Base in Tampa, Florida, USA. A total of ten flights (3-8 hours each) at 20 km altitude were performed. Each flight spent 3-4 hours above active thunderstorms. Extended Data 10 shows an overview of the flight dates, durations, target locations, and total number of observed glow episodes and gamma-ray glows.

The science goals of ALOFT were the observation of Terrestrial Gamma-ray Flashes (TGF) and gamma-ray glows from thunderstorms and the study of their connection. The airborne scientific payload consists of five independent gamma-ray detectors, 30 photometers, three electric field sensors, two radars and two passive radiometers. In addition, nine ground-based radio receivers were operated during the campaign, covering Very Low Frequencies (VLF), Low Frequencies (LF) and Very High Frequencies (VHF), including two interferometers and one Lightning Mapping Array (LMA). The instruments used in this study are described in Methods Section 2.

A key feature of the mission was the near real-time downlink of one-second time resolution gamma-ray count rates. This enabled the immediate identification of gamma-ray glowing thunderclouds, and the pilot was instructed to return on the same location as long as gamma-ray glows were detected.

2. INSTRUMENTATION

The Bismuth-Germanate instrument from the University of Bergen (UIB-BGO).
This instrument consists of four independent gamma-ray detectors; one Bismuth Germanate (BGO) detector, with three independent BGO crystals with Photomultiplier Tube (PMT) readout, and three LYSO detectors. All detectors have different geometric areas ranging from 0.09 cm^2 to 225 cm^2, in order to provide four orders of magnitude dynamic range in flux. In fact, modelling work[29] showed that the flux from a typical TGF observed at 20 km altitude can vary by 4 orders of magnitude, depending on the radial distance from the source to the aircraft. The three BGO/PMT detectors are similar in design and readout architecture to one of the four High Energy Detector modules of the Modular X- and Gamma-ray Sensor (MXGS)[30] onboard the Atmosphere Space Interaction Monitor (ASIM) on the International Space Station (ISS). The three BGO/PMT detectors have a total geometrical area of 225 cm2, are sensitive in the energy range 300 keV - >30 MeV, and have a 28 ns time-tagging accuracy. In this work we use only data from the BGO detectors. Additional information on UIB-BGO can be found in the companion paper[24].

The in-Situ Thunderstorm Observer for Radiation Mechanisms (iSTORM),
iSTORM is a gamma-ray spectrometer designed and built by the US Naval Research Laboratory for the measurement of bright, fast transients in the energy range ~300 keV - >5 MeV). iSTORM consists of an array of 32 1-inch diameter $CeBr_3$ scintillating crystals with Silicon Photomultiplier (SiPM) readout, with temporal resolution <1μs, for a total

* FEGS = Fly´s Eye GLM Simulator, GLM=Geostationary Lightning Mapper

geometrical area of 157 cm^2. The large area provides high sensitivity, while the high segmentation and fast scintillation decay time provides robustness towards potential detector paralization from bright TGFs. Additional information on iSTORM can be found in the companion paper[24].

The Advanced Microwave Precipitation Radiometer (AMPR)

The Advanced Microwave Precipitation Radiometer (AMPR) is a cross-track scanning radiometer that passively measures total power at 10.7 GHz, 19.35 GHz, 37.1 GHz, and 85.5 GHz[31]. The instrument uses a rotating splash plate mirror to focus microwave energy into its feedhorns. This causes the polarization of the incoming signal to vary sinusoidally as a function of scan angle. AMPR has two orthogonally polarized channels per frequency, so it is possible to retrieve fully vertical and fully horizontal polarizations by deconvolving the orthogonal measurements at each frequency. At ER-2 altitudes, AMPR's instantaneous field-of-view (IFOV) resolution varies between 0.6-2.8 km, with the finest resolution associated with 85.5 GHz and the coarsest resolution associated with 10.7 GHz. AMPR's swath is ~38 km wide when flying at 20 km altitude on the ER-2. AMPR completes a cross-track scan in ~2.5 seconds, and after 5 scans the instrument collects measurements of two blackbodies – a heated hot load and an air-cooled cold load – to enable calibrated brightness temperature (TB) retrievals.

AMPR TBs are first retrieved using a simple two-point linear method that compares scene radiometer counts to the radiometer counts from the hot load (typically ~320 K) and from the cold load (which can reach a minimum temperature of ~240 K during a flight). With most meteorological scenes, this methodology is capable of producing well-calibrated TBs suitable for quantitative geophysical retrievals[31]. However, during ALOFT it was found that, due to the large amount of ice scattering observed in these storms, a linear assumption was not suitable for the 85-GHz channels, as the scene targets were so radiometrically cold that receiver response entered a nonlinear regime. Thus, AMPR 85-GHz TBs were corrected for receiver nonlinearity using a simple gain adjustment factor which became stronger as scene counts went lower than cold load counts, and thus prevented negative TB retrievals. This correction also reproduced 85-GHz TBs that were within approximately +/- 10 K of previous AMPR observations of intense convection[32-33] and that remained highly correlated with 85-GHz scene counts (Pearson correlation coefficient > 0.9). The corrected 85-GHz TBs are thus suitable for qualitative identification of significant precipitation cores and the presence of ice scattering.

The ER-2 X-band Radar (EXRAD)

The ER-2 X-band radar (EXRAD) is an X-band (9.6 GHz) precipitation radar and scatterometer that flies in the ER-2 nose and it is used for measuring both the three-dimensional precipitation structure and surface winds. It has a fixed nadir beam and a conical scanning beam that is tilted approximately 30 degrees off nadir. EXRAD measures radar reflectivity, Doppler velocity, and Doppler spectral width. It was first flown in 2014. EXRAD uses a 0.66-m diameter slotted waveguide antenna with a single linear polarization for the scanning beam plus a second 0.66-m linear polarized slotted waveguide antenna for a nadir beam. This ~ 3.4 degree beam provides a beamwidth of approximately 0.6 km at 10 km altitude, and 1.2 km at the surface. EXRAD calibration is performed using the ocean surface, and current Doppler processing includes non-uniform beam filling (NUBF) corrections for artifacts caused by the aircraft motion. Calibration accuracy is better than 1 dBZ for reflectivity and <1 ms^{-1} for Doppler. More details on EXRAD hardware and processing can be found in[34].

The Lightning Instrument Package (LIP)

The Lightning Instrument Package (LIP) consists of seven rotating vane electric field mills installed on the NASA ER-2 aircraft to observe the total vector electric field and vector electric field (Ex, Ey, Ez) generated by cloud charging and lightning discharges[35-38]. LIP measures the vector electric field in the atmosphere and the charge induced on the aircraft using the processing and calibration technique in[39]. The individual laboratory dynamic range for the mills is ± 1.75 V m^{-1} to 920 kV m^{-1}. Properly calibrated on the aircraft, LIP can reliably measure fields lower than 1 V m^{-1} and as high as 512 kV m^{-1} with 0.1 s temporal resolution. Effects on the derived vertical electric field due to aircraft charging are generally 5% or less, with a maximum upper error of 10%[36]. Both aircraft relative and Earth relative frameworks are determined, and the total electric field magnitude is then computed from the vector components.

The Electric Field Change Meter (EFCM)

The Electric Field Change Meter (EFCM) is a two-channel (fast and slow) antenna that measures the derivative of the electric field impulse produced by lightning. The fast channel is designed to isolate the radiative component of the lightning discharge field while the slow channel is optimized to observe the electrostatic field component. The EFCM has multiple sensitivity ranges that are selectable during flight and samples with 16-bit resolution. The EFCM trigger rate shown in Extended Data 2 and 4 is clipped at a maximum of ten triggers in ten seconds. This is because an EFCM trigger implies acquisition of one-second data around the trigger time. Such rate is therefore the maximum trigger rate possible, implying nearly continuous data recording. The real discharge rate may be much higher. Additional information on EFCM can be found in the companion paper[24].

The Central Florida Lightning Mapping Array (CFLMA)

The Central Florida Lightning Mapping Array (CFLMA) consisted of 6 widely-spaced VHF stations that receive the VHF radiation produced by lightning in a 6 MHz bandwidth between 60 and 66 MHz (U.S. TV Channel 3). Each station detects the peak radiation event above a local threshold value in successive 80 microsecond time windows with 40 ns time resolution and utilizes the arrival times at the different sites to locate the sources of impulsive radiation sources in 3 spatial dimensions and time, as well as the VHF source powers. Owing to logistical and sensitivity issues, a small number of events were detected per flash, but these were sufficient both for obtaining the basic location of individual flashes and for determining the overall electric charge structure of the storms. Important high-power events were well-detected and located by the network.

Advanced Baseline Imager (ABI)

This work makes use of public data from the Advanced Baseline Imager (ABI) instruments onboard the GOES-16 and GOES-18 geostationary satellites. ABI provides radiometric measurements in 16 spectral bands from the visible (0.47 μm) to the infrared (13.3 μm), with spatial resolution from 0.5 km (visible) to ~2 km (infrared). The temporal resolution depends on the ABI operational mode. For seven flights out of ten, the ALOFT mission was granted a dedicated Mesoscale Domain Sector (MDS) which provides scans of a 1000x1000 km^2 box every 60 seconds. For the three flights over Florida, we made use of the Continental US (CONUS) scans, which are provided every five minutes. In this work we use radiance measurements in the ABI band 13 (infrared, 10.3 μm) which are then converted to brightness temperatures by applying the Planck function and a spectral bandpass correction according to the GOES-R Series Product Definition and Users' Guide[40].

3. DURATION AND EXTENSION OF GAMMA-RAY GLOW ACTIVITY

In this section we present information on two other flights: 06.07.2023 over Campeche Bay, and 29.07.2027 over Florida. In addition to the very active storm on 24.07.2023 the other two case studies (shown here), as well as the 6 other storms all show that the novel findings of this paper (hour-long durations, large spatial extension of gamma-ray activity, significant variability on second to millisecond timescales) are common features also in less severe storms.

For all case studies we present time-based color-coded maps and gamma-ray sequences (Extended Data 1 and 3) which provide a visualization of gamma-ray data alternative to that presented in Figure 1 in the main text. Here the reader can match a specific glow episode with a position on the map based on the highlight color. In addition, we provide gamma-ray count rate with simultaneous electric field and cloud characterization data for selected time intervals (Extended Data 2 and 4). These figures show the same observation pattern presented in Figure 3 in the main text: glow episodes, each of them comprising several individual glows, are observed during the overpass of convective cores with large radar reflectivity, implying large liquid and ice contents as well as strong convective updrafts at high altitudes. In all cases, the upward-pointing electric field vectors are consistent with the presence of an upper positive charge layer. In addition, Extended Data 2 and 4 show EFCM trigger rate which peaks during the passage over gamma-ray active convective cores. EFCM data were not available for the flight on 24.07.2023.

In the following we report additional information for the case-study flights on 06.07 and 29.07.

a) Flight on 06.07.2023

The target area showed developing multicell convection that evolved into a MCS at the time of overflight. The area is Campeche Bay, same as for the flight on 24.07.2023 discussed in the main text. This storm represents a very clean case illustrating the large spatial extension and long duration of a gamma-ray glowing thundercloud region. Extended Data 1 shows six consecutive passes over the same core region, each associated with glow episodes (Extended Data 2). The total time span of these passes is 40 minutes, which represents a lower limit of the duration of the glow activity. The overall spatial extension of the glowing region is about 600 km^2.

b) Flight on 29.07.2023: comparison with lightning activity and storm charge structure.

The flight over east-central Florida on July 29 produced observations similar to those obtained over the Central America coastal areas, but included important observations of VHF radiation from the 3-D Central Florida Lightning Mapping Array (CFLMA) over the area. The Florida storm cells were more localized than those of the other flights and produced relatively well-separated glows, as seen in Extended Data 3 and 4. Extended Data 3 shows seven consecutive passes over the same ~400 km^2 core region, each of them resulting in significant glow episodes, for a total duration of about one hour.

The strongest episode occurred at 20:30:30 UT (Extended Data 3b), and is shown in detail in Extended Data 5, which compares the glow sequence with LMA observations of the lightning activity. The episode consisted of three glows, the last one much dimmer than the others. Here we focus on the first two glows, each of which was rapidly quenched at the time of an intracloud lightning flash in the storm. The glows were noticeably different from each other, with the first glow lasting 8 seconds and being detected as the ER-2 entered the periphery of the electrically active storm from the northeast (top horizontal arrow in panel 8c). In contrast, and by sheer chance, the second glow occurred 20 seconds later when the ER-2 was directly above the central part of the storm and the flash that terminated the glow. Instead of increasing linearly with time, as in the first glow, the second glow grew exponentially for 4 seconds to twice the count rate of the first glow (namely to ~20,000 per second), at which point a highly energetic intracloud flash was initiated that quenched the glow (red sources in the panels of Extended Data 5, with the ER-2 location indicated by the bottom horizontal arrow). That the quenching flash was energetic is indicated by two of the initial LMA sources having extremely strong VHF powers of 53.9 and 52.9 dBW, or ~200 kW. (The quenching flash for the first glow had moderate source powers, and corresponded to the light green sources in the same plan area and altitude range as the subsequent red sources in Extended Data 5c.)

Extended Data 6 shows the lightning-inferred charge structure around the time of the 20:30 glows, showing that the storm had a normal-polarity tripolar structure, with upper positive charge between ~13-15 km and mid-level negative charge at ~9-12 km, and confirming that the first glow was observed on the periphery of both charge regions, while the second glow was observed directly above the core. The polarity is inferred by virtue of intracloud flashes producing higher-power RF-noisy negative polarity breakdown through the storm's upper positive charge, and less noisy positive breakdown within the storm's mid-level charge[41].

4. MONTE CARLO SIMULATIONS

Using Monte Carlo simulations, we can evaluate certain theoretical characteristics of gamma-ray glows. It is anticipated that all observed spectra originate from the Relativistic Runaway Electron Avalanche (RREA) process. We utilized the GEANT4 software[42], which enables the simulation of photon, electron, and positron propagation in the atmosphere. The simulation initiates with a point source of upward-pointing electrons, with a classical RREA energy spectrum up to 40 MeV at the source[43]. The simulations follow the following steps: 1) Propagation, scattering, and absorption of RREA electrons in the atmosphere, along with the generation and propagation of secondary Bremsstrahlung photons from various altitudes (ranging from 8 to 16 km). 2) The recording of photons at an altitude of 20 km, which corresponds to the altitude of the aircraft. 3) These point source simulations are extended by random sampling to generate any extended source.

a) Attenuation with radial distance

Here we estimate how far away from the aircraft nadir can gamma-ray glows be detected by ALOFT. We can safely identify dim glows which exhibit a minimum count rate increase of 25% above the background level (using one-second time bin). Conversely, the brightest glows exhibit a count rate up to ~12 times the background (using one-second time bin). We therefore detect glows with maximum intensity spanning a dynamic range of ~50. This observed dynamic range includes both contributions from the intrinsic glow intensity variability, and absorption due to the source location with respect to the aircraft. Extended Data 7 shows the expected number of photons per unit area at 20 km altitude for sources at different altitudes and radial distance from the aircraft, normalized to 1 at radial distance 0. The dashed horizontal line marks the detection threshold (0.02, following from a dynamic range of 50). Assuming that the brightest glows are detected from sources close to the nadir, we can see that a source as bright would be detectable at 25% above the background level up to 2 – ~4.5 km radial distance, depending on the source altitude. Considering that glows are detected while passing over convective cores extending at high altitudes, it is likely that the sources have a high altitude as well (see discussion of the cloud charge structure in Methods 3b) therefore the detection range is likely lower than ~3.5 km.

b) Time profile due to aircraft motion

Here we estimate the observed time profile of a stationary gamma-ray glow due only to the aircraft motion. Extended Data 8 shows the relative number of counts at aircraft altitude assuming the aircraft is flying towards an extended source (7.5 km radius disk) at 16 km altitude for different radial offsets. The rise time from 2% (detection threshold assuming the dynamic range 50 discussed in Method 4a) to 95% of the maximum is >18 seconds. This is way longer than the typically observed rise times (2-4 s) suggesting that the intrinsic time variability of the source dominates the observed time profile. This rise time further increases with increasing radial offset from the source. The relative intensity sharply decreases when the radial offset exceeds the physical extension of the glow region, in agreement with the attenuation with radial distance discussed above in Method 4a.

c) Glow spectral analysis

Here we show that the energy spectra of a sample of the detected gamma-ray glows can be well modeled by the RREA process. Extended Data 9a presents energy spectra and lightcurves for four cases detected during the flight on 06.07.2023. It also includes the best fit results from a RREA model, which closely matches the observed glow spectra. The fitting procedure involved the following steps:

1. Start with an upward electron source at 15 km altitude, with a typical RREA electron energy spectrum.
2. Propagating these electrons through the atmosphere and recording bremsstrahlung photons at 20 km altitude (only a negligible fraction of electrons reach this altitude).
3. Applying the response matrix of the BGO instrument to simulate the spectrum and subsequently comparing it with the observed data.

For the best fit, we utilized an averaged spectrum derived from all the observations shown. A key parameter optimized in this modeling was the extent of the RREA region. The best fit was achieved with a source region larger than 8 km spatial extent, determined using a maximum likelihood approach. Although the approach is potentially mixing sources with different characteristics, it shows that the RREA process is a good explanation for the observed gamma-ray glow spectra.

With the same procedure we also performed spectral analysis of the glow burst detected on 24.07.2024 at 06:44:59.182 UTC and presented in Figure 2f. Extended Data 9b presents the energy spectrum for this event. The spectrum can be well fit with a RREA model and does not show any evidence of enhanced features at the 511 keV positron annihilation line. Therefore, we conclude that this event is intrinsically different from the positron bursts presented in[23].

REFERENCES

29. Hansen, R.S., et al., *How simulated fluence of photons from terrestrial gamma ray flashes at aircraft and balloon altitudes depends on initial parameters.* Journal of Geophysical Research: Space Physics, **118**(5): p. 2333-2339 (2013).
30. Østgaard, N., et al., *The Modular X- and Gamma-Ray Sensor (MXGS) of the ASIM Payload on the International Space Station.* Space Science Reviews, **215**(2) (2019).
31. Amiot, C.G., et al., *Dual-Polarization Deconvolution and Geophysical Retrievals from the Advanced Microwave Precipitation Radiometer during OLYMPEX/RADEX.* Journal of Atmospheric and Oceanic Technology, **38**(3): p. 607-628 (2021).
32. Leppert, K.D. and D.J. Cecil, *Signatures of Hydrometeor Species from Airborne Passive Microwave Data for Frequencies 10–183 GHz.* Journal of Applied Meteorology and Climatology, **54**(6): p. 1313-1334 (2015).
33. Battaglia, A., et al., *Using a multiwavelength suite of microwave instruments to investigate the microphysical structure of deep convective cores.* Journal of Geophysical Research: Atmospheres, **121**(16): p. 9356-9381 (2016).
34. Heymsfield, G.M.L.L.M.W.M.C.H.S.G., *NASA Airborne Radars for Studying Clouds and Precipitation.* Advances in Weather Radar, **1**: p. 231-282 (2024).
35. Bateman, M.G., et al., *A Low-Noise, Microprocessor-Controlled, Internally Digitizing Rotating-Vane Electric Field Mill for Airborne Platforms.* Journal of Atmospheric and Oceanic Technology, **24**(7): p. 1245-1255 (2007).
36. Mach, D.M., et al., *Electric fields, conductivity, and estimated currents from aircraft overflights of electrified clouds.* Journal of Geophysical Research: Atmospheres, **114**(D10) (2009).
37. Mach, D.M., et al., *Comparisons of total currents based on storm location, polarity, and flash rates derived from high-altitude aircraft overflights.* Journal of Geophysical Research: Atmospheres, **115**(D3) (2010).
38. Schultz, C.J., et al., *Remote Sensing of Electric Fields Observed Within Winter Precipitation During the 2020 Investigation of Microphysics and Precipitation for Atlantic Coast-Threatening Snowstorms (IMPACTS) Field Campaign.* Journal of Geophysical Research: Atmospheres, **126**(16) (2021).
39. Mach, D.M. and W.J. Koshak, *General Matrix Inversion Technique for the Calibration of Electric Field Sensor Arrays on Aircraft Platforms.* Journal of Atmospheric and Oceanic Technology, **24**(9): p. 1576-1587 (2007).
40. *GOES R SERIES PRODUCT DEFINITION AND USERS' GUIDE (PUG)*. 2019. p. 27-28.
41. Thomas, R.J., et al., *Observations of VHF source powers radiated by lightning.* Geophysical Research Letters, **28**(1): p. 143-146 (2001).
42. Agostinelli, S., et al., *Geant4—a simulation toolkit.* Nuclear Instruments and Methods in Physics Research Section A: Accelerators, Spectrometers, Detectors and Associated Equipment, **506**(3): p. 250-303 (2003).
43. Dwyer, J.R., *A fundamental limit on electric fields in air.* Geophysical Research Letters, **30**(20) (2003).

DATA AVAILABILITY

All the data used in this study are available on ZENODO Repository, doi: 10.5281/zenodo.12531291. The description of the formats is uploaded in the file: Data_description.pdf

CODE AVAILABILITY

References to software tools and codes for this study are given in the file: Data_description.pdf, which is uploaded to the ZENODO Repository, doi: 10.5281/zenodo.12531291.

EXTENDED DATA FIGURES AND TABLES

Extended Data 1.
Time-based color-coded map and gamma-ray sequence for the flight on 06/07/2023 (Campeche Bay): 06.07.2023 04:25 UT – 07:05 UT.
a) Flight trajectory (grey) overlaid on GOES-18 infra-red temperatures, along with marked gamma-ray fluxes exceeding 25% above the background level. The brightness temperature cloud image corresponds to time 05:00:30 UT. b) BGO count rate. Gamma-ray fluxes exceeding 25% above the background level are color-coded based on time from 04:25:00 UT, correspondingly in panels a and b.

Extended Data 2
Gamma-ray count rate with simultaneous electric field and cloud characterization data for flight on 06.07.2023, 04:57 – 05:20 UT.
a) BGO count rate (black, left vertical axis) and EFCM trigger rate (red, right vertical axis). b) Brightness Temperature (TB) from AMPR 85.5 GHz Channel A. Sweep Index 0 (49) corresponds to scan direction 45 degrees from Nadir towards starboard (port). C) vertical radar reflectivity profile from EXRAD. Black vectors are the E_{xz} component of the electric field from LIP, where x-axis is the direction of motion and z-axis is the upward-pointing vertical direction. AMPR, EXRAD and LIP data are not shown if roll angle is larger than 2 degrees (aircraft maneuvering).

Extended Data 3
Time-based color-coded map and gamma-ray sequence for the flight on 29/07/2023 (Florida, east coast): 29.07.2023 19:55 UT – 21:05 UT.
a) Flight trajectory (grey) overlaid on GOES-16 infra-red temperatures, along with marked gamma-ray fluxes exceeding 25% above the background level. The brightness temperature cloud image corresponds to time 20:31:17 UT. b) BGO count rate. Gamma-ray fluxes exceeding 25% above the background level are color-coded based on time from 19:55:00 UT, correspondingly in panels a and b.

Extended Data 4
Gamma-ray count rate with simultaneous electric field and cloud characterization data for flight on 29.07.2023, 20:28 – 20:50 UT.
a) BGO count rate (black, left vertical axis) and EFCM trigger rate (red, right vertical axis). EFCM data were lost between 20:45:44 and 20:56:00 due to a system failure. b) Brightness Temperature (TB) from AMPR 85.5 GHz Channel A. Sweep Index 0 (49) corresponds to scan direction 45 degrees from Nadir towards starboard (port). c) vertical radar reflectivity profile from EXRAD. Black vectors are the E_{xz} component of the electric field from LIP, where x-axis is the direction of motion and z-axis is the upward-pointing vertical direction. AMPR, EXRAD and LIP data are not shown if roll angle is larger than 2 degrees (aircraft maneuvering).

Extended Data 5

LMA observations for the energetic two-pulse glow event at 20:30 UT on 29.07.2023.

a) Temporal comparison of the 1-second averaged BGO count rate (blue line and red + signs) with the occurrence of lightning in the storm (square dots, colored by time), c) Plan view of the LMA sources and ER-2 trajectory (blue diagonal line from northeast to southwest), showing the location of the ER-2 at the time of the glows (horizontal arrows) relative to the LMA sources (black lines show coastal and inland water boundaries around Kennedy Space Center, green squares show locations of two LMA stations), b,d) North-south and east-west vertical projections of the LMA sources and the spatial extent of the glows and the height of the ER-2 relative to the lightning, e) histogram of the source altitudes.

Extended Data 6

Lightning-inferred charge structure around the time of the 20:30 glows.

Same as Extended Data 5, except showing the typical tri-polar structure (main mid-level negative (blue) and upper positive charges (red-orange), and weaker lower positive charge) over a five minute interval around the time of the glow sequence.

Extended Data 7

Gamma-ray glow detectability.

Expected number of photons per unit area at 20 km altitude (Arbitrary Units, normalized to 1 at radial distance 0) for sources at different altitudes and radial distance from the aircraft. Assuming a maximum intensity of ~12 times the background for glows detected at radial distance 0 (the maximum observed intensity) the dashed horizontal line marks the detection threshold for gamma-ray glows 25% above the background.

Extended Data 8

Count rate variability due to aircraft motion.

Relative number of counts at aircraft altitude assuming the aircraft flying toward an extended source (7.5 km radius disk) at 16 km altitude for different radial offsets.

Extended Data 9

Gamma-ray glow and glow burst spectra.

a) Background-subtracted differential energy spectra for four time intervals including several glows detected on 06.07.2023. Error bars are one standard deviation. The insets show the BGO count rates. The corresponding time intervals (start time – stop time, UTC) are: glow 4 05:00:49 – 05:03:07, glow 5 05:07:09 – 05:09:20, glow 7 05:23:35 – 05:24:13, glow 10 06:51:13 – 06:52:33. b) Background-subtracted differential energy spectra for the glow burst detected on 24.07.2024 at 06:44:59.182 UTC. Error bars are three standard deviations.

Extended Data 10.

ALOFT flights summary table.

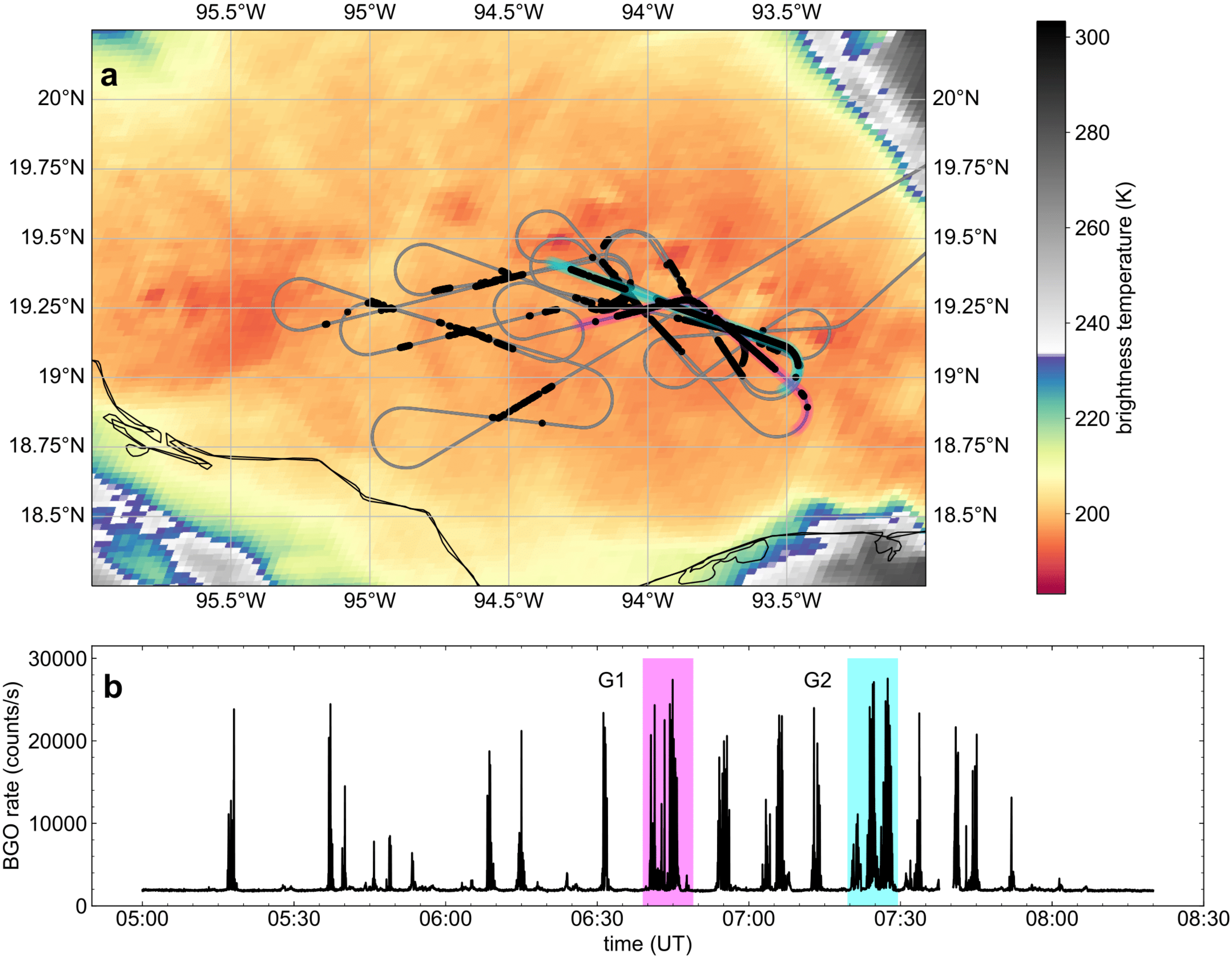

a
95.5°W
95°W
94.5°W
94°W
93.5°W
20°N
19.75°N
19.5°N
19.25°N
19°N
18.75°N
18.5°N
brightness temperature (K)
300
280
260
240
220
200
b
G1
G2
BGO rate (counts/s)
30000
20000
10000
0
05:00
05:30
06:00
06:30
07:00
07:30
08:00
08:30
time (UT)

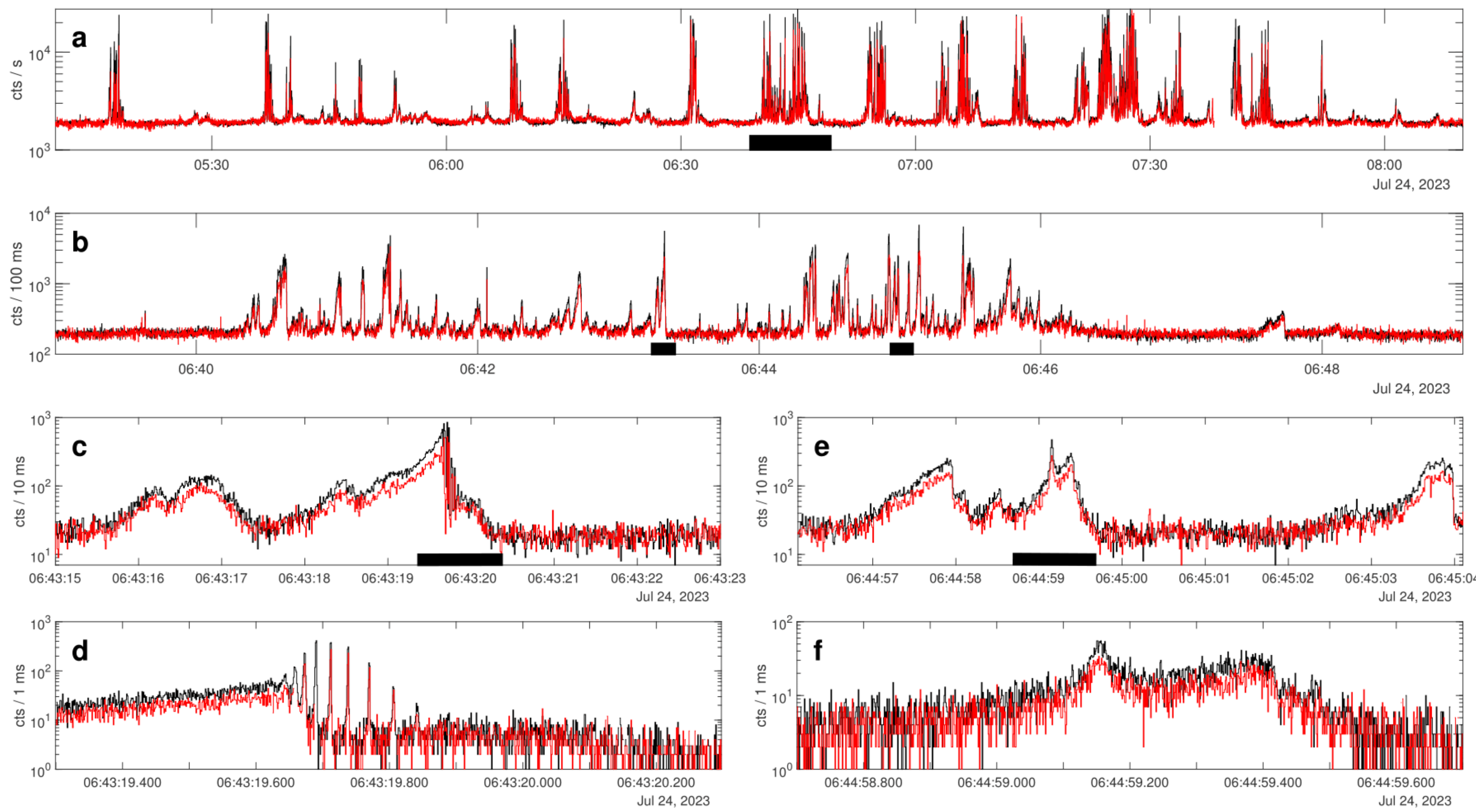

a
b
c
d
e
f
cts / s
cts / 100 ms
cts / 10 ms
cts / 1 ms
05:30
06:00
06:30
07:00
07:30
08:00
06:40
06:42
06:44
06:46
06:48
06:43:15
06:43:16
06:43:17
06:43:18
06:43:19
06:43:20
06:43:21
06:43:22
06:43:23
06:44:57
06:44:58
06:44:59
06:45:00
06:45:01
06:45:02
06:45:03
06:45:04
06:43:19.400
06:43:19.600
06:43:19.800
06:43:20.000
06:43:20.200
06:44:58.800
06:44:59.000
06:44:59.200
06:44:59.400
06:44:59.600
Jul 24, 2023